Earthquake Damage Scenario in Visp (Switzerland): From Active Fault to Building Damage

J. Burjánek, D. Fäh, C. Michel, L. Dalguer, C. Baumann, G. Gassner-Stamm, V. Poggi & D. Roten
Swiss Seismological Service, ETH Zürich, Zürich, Switzerland

J. Laue & A. Marin
Institute of Geotechnical Engineering, ETH Zürich, Zürich, Switzerland

P. Lestuzzi & A. Karbassi
Applied computing and Mechanics Laboratory, EPF Lausanne, Lausanne, Switzerland

SUMMARY:
We present a damage scenario based on multidisciplinary study which covers the key elements of the earthquake risk chain in Visp. Full dynamic rupture simulations are performed using heterogeneous initial distributions, statistically compatible to the database of kinematic inversion results of past earthquaks. The fault is embedded in the 3D velocity model of the area, which is based on an extensive ambient noise measurement campaign. In order to assess the risk in the city of Visp, the buildings were classified based on the screening survey of the building stock. The seismic behavior of each class is described by the mean of fragility curves, partly developed by analytical, numerical and experimental investigations and partly based on existing methods.

Keywords: Earthquake scenario, Numerical modelling, Strong ground motion

1. INTRODUCTION

The Valais is the area of greatest seismic hazard in Switzerland and has experienced a magnitude 6 or larger event every 100 years. Due to river regulations and engineering progress in the last two centuries, seismically unfavorable sites have become attractive for expanded settlement and industries, so the seismic risk has potentially increased (Fig. 1.1). The area of the city of Visp is of special interest, since damaging earthquakes occur on average every 40 years (Intensity VI-VIII). It is located on deep sediment-filled valley, which consists of horizontally layered fluvial deposits of the Rhone river. The significant earthquake damage was reported in the past resulting either directly from strong ground motion, or from different secondary phenomena including liquefaction and ground failure of the Rhone plain (Fritsche et al., 2006). As there are no available instrumental observations of these phenomena for the region, physics-based numerical modeling is required to adequately assess potential future events. We present detailed damage scenarios based on multidisciplinary study which covers the key elements of the earthquake risk chain in Visp. These key elements are: (1) identification of the active faults in the area, (2) numerical simulation of the dynamic ruptures along these faults, (3) simulation of the seismic wave propagation in the 3D velocity model, (4) simulation of the non-linear soil response close to the surface, and (5) quantitative estimation of the building damage resulting from simulated ground motions. In particular, the active fault survey is guided by geological observations, evaluation of the recent seismic activity, current geodetic surveys, and ambient vibration surveys, which are performed to map potential fault zones. Full dynamic rupture simulations are performed using heterogeneous initial distributions, statistically compatible to the database of kinematic inversion results of past earthquakes. The fault is embedded in the 3D velocity model of the area, which is based on an extensive ambient noise measurement campaign. Top-most stratigraphic layers include water saturated silty-sand layers, which are prone to liquefaction. A set of laboratory tests has been performed on undrained samples to establish relevant input parameters needed for non-linear soil models (Roten et al., 2009). Furthermore, a borehole site has been identified in Visp, which will be equipped with seismic
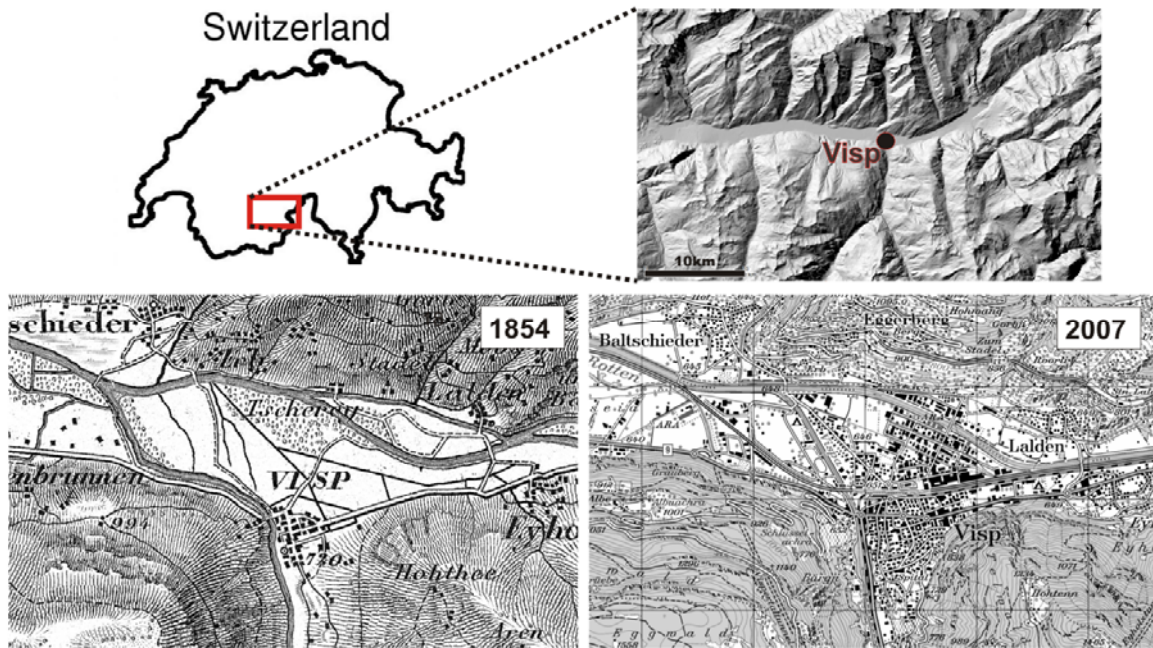
Figure 1.1: Location of Visp within the Rhone valley (relief map at top), and the development of the Visp area in last 150 years.

instruments (at several depths), strain-meters, and pore pressure sensors. The installation will be finished during 2012, and should provide additional constraints on the soil response. In order to assess the risk in the city of Visp, the buildings were classified based on the screening survey of the building stock. The seismic behavior of each class is described by the mean of fragility curves. The curves for certain classes were especially developed for Switzerland using analytical, numerical and experimental investigations. The other classes were described using the existing vulnerability assessment of Lagomarsino and Giovinazzi (2006).

2. DEVELOPMENT OF THE VELOCITY MODEL

An extensive ambient noise measurement campaign was performed in the area (13 small-aperture arrays, almost 150 single-station measurements; see Fig. 2.1). The aim of the array measurements was to constrain the average shear-wave velocity of the main geological layers, identify the key interfaces, and map the lateral velocity variations. Single-station measurements were used after to map changes in the interface depth between the layers. Array measurements were processed by means of a three-component, high-resolution f-k method estimating both Love and Rayleigh dispersion curves (Fäh et al., 2008). The ellipticity of Rayleigh waves was estimated for all array measurements by both new array-based (Poggi and Fäh, 2010) and wavelet-based techniques (Fäh et al., 2009). Locally 1D velocity profiles were finally obtained by joint inversion of the dispersion curves and Rayleigh wave ellipticities. The inversion of 1D velocity profiles was performed using the Dinver software that implements the modified Neighborhood Algorithm (Wathelet, 2008).

Summarizing the results for the arrays (not presented here, see Burjanek et al., 2010, Burjanek et al. 2011), shear wave velocities reach 150-200 m/s in the shallowest layers (<20 m). These layers are variable in thickness and velocity throughout the city, and we measured the variability in composition of these surface sediments. Bellow these low-velocity layers the shear wave velocity increases gradually to 300-500 m/s, reaching the strong interface at the depth of 40-60 m (shear wave velocity increases here up to factor of three). This interface was identified by all arrays in the area, and linked to the transition from sands and gravels to compacted moraine. The resolution of the shear wave velocities is limited bellow this interface, so the bedrock depth is not resolved by the array measurement at all (though, it is necessary to consider deep bedrock to fit the observed amplification factors, Burjanek et al., 2011).
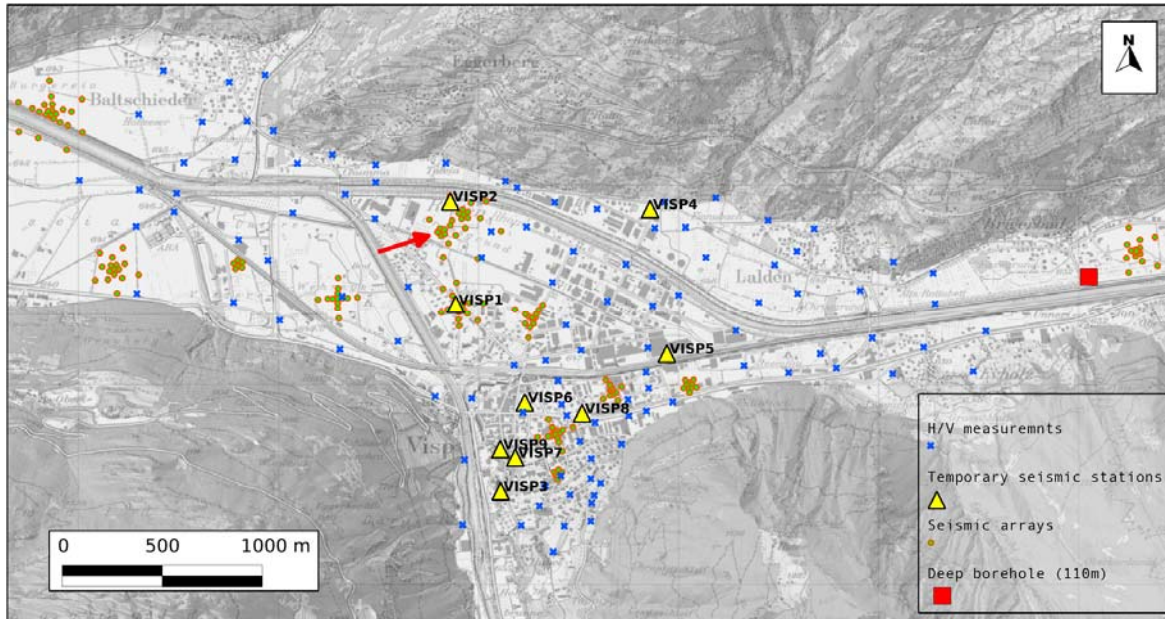
Figure 2.1: Overview of measurements performed in the Visp area. Ambient noise array measurements are shown as green dots, single-station measurements as blue crosses, temporary stations as yellow triangles. Red square indicates the location of only deeper borehole (~110 m) in the area. Red arrow points at the location of planned borehole site (five boreholes 15-150 m), which will be instrumented by several seismic, deformation and pore-pressure sensors.
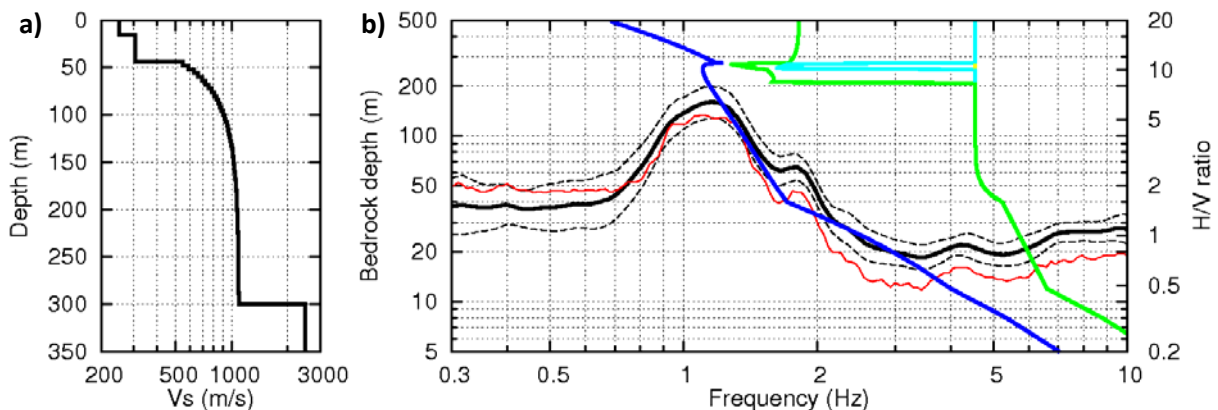

Figure 2.2: An example of the velocity profile at one point in the basin (a). The upper part of the profile (depth < 60 m) is constrained by ambient noise array measurements. The bedrock depth is estimated from the H/V single station measurements (b): average H/V noise ratio (solid black), +/- standard deviation (dashed black), Rayleigh wave ellipticity by wavelet transform (red), frequency-to-depth relations assuming 1st (blue), 2nd (green) and 3rd (cyan) peak of the ellipticity of the Rayleigh fundamental mode. A depth of 300 m was picked in this example.

In order to estimate the full basin geometry, we generalized a two step procedure described by Poggi et al. (2012). In first step, shallow velocity structure (depth <50 m) was estimated by direct interpolation of the results from the array survey. In particular, the depths of the two first interfaces (~20m, ~50m, see Fig. 2.2 left) were interpolated using the kriging method and assuming constant velocity in the two layers. In the second step, we estimated the bedrock depth by fitting the fundamental frequencies measured at 150 different sites with the single station noise measurements. In particular, we assume a gradual velocity increase bellow the second interface (Fig.2.2a). Next, we were progressively changing the depth of the bedrock and calculating the frequency of the Rayleigh wave ellipticity peak. In this way, we built a frequency-depth relation for each site of the H/V measurement (e.g., blue curve in Fig. 2.2b). Finally, we pick the depth of the bedrock directly from the
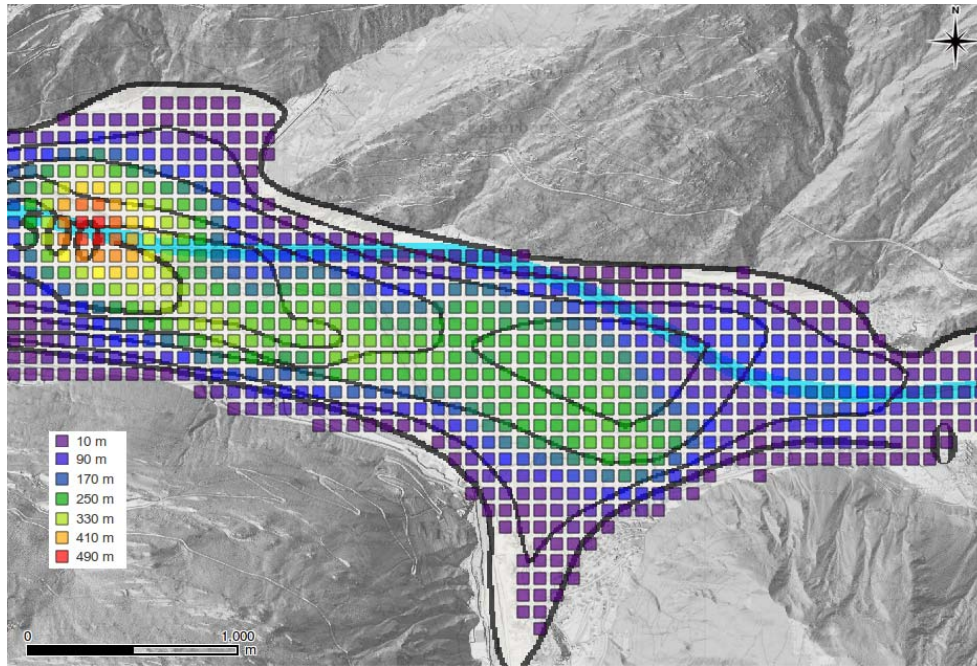
Figure 2.3: Interpolated depth of the bedrock from the H/V single station measurements (in color). Black contours represent the bedrock depth from the independent gravimetric study.

joint plot of the H/V curve and frequency-depth relations (Fig. 2.2b). Such relatively complicated procedure provided more robust results, since number of the H/V curves contained plateaus and multiple peaks which are hard to be interpreted alone (difficult to pick a single fundamental frequency). The presence of the several strong interfaces in the shear wave velocity profile makes the bedrock depth estimation difficult. For example, the synthetic ellipticity of the fundamental mode contained several peaks, thus we got several frequency-depth relations (blue, green, cyan curves in Fig. 2.2b). Usually, for a certain bedrock depth range, the three peaks collapse to a single strong peak (250 -280 m in Fig. 2.2b), what explains, that we observe strong peaks at some of the stations. Moreover, relatively fast consolidated sediments in the lower layer make the fundamental frequency extremely sensitive to the bedrock depth (Fig. 2.2b). In other words, a small error in the fundamental frequency results in a great error in the bedrock depth. The interpolated bedrock depth is presented in Fig. 2.3, and is in good agreement with the recent gravimetric study (Rosselli, 2001).

Longitudinal wave velocity was calculated from the shear wave velocity using mean Poisson's ratio profile obtained from the array measurements. Shear wave velocity of the bedrock was taken from the regional tomographic studies. Density profile was prescribed according Rosselli (2001). Quality factor of the uppermost layer was estimated by a trial-and-error (fitting observed site-to-reference spectral ratio at one of the temporary stations with 1D transfer function). Finally, quality factor of sediments at deeper depths was taken from Roten et al. (2008).

3. DEVELOPMENT OF THE SOURCE MODEL

The canton Valais is the most seismically active area in Switzerland. Marschall and Deichmann (2012) reviewed the seismotectonics of the area, and provided an update on the stress orientations. Moreover, Baumann (2012) collected existing information on active faults in Valais, and listed faults which might be responsible for the 1855 M6.2 Visp earthquake. In this study, we have focused on a normal fault south to Visp (Fig. 3.1, Strike=180°, Dip=45°, Rake=-90°). There are several indications for the existence of this fault including: 1) geological field observation on the surface (Werenfels, 1924); 2) observation in the intersecting tunnel construction; 3) field observations of possible co-seismic displacements in the area (Joris 2010, personal communication); 4) geophysical ambient vibration survey, which identified potential fault gauge (Baumann, 2012). Moreover, the damage field of the 1855 M6.2 earthquake (Fritsche et al., 2006) is in rough agreement with the geometry of this fault.
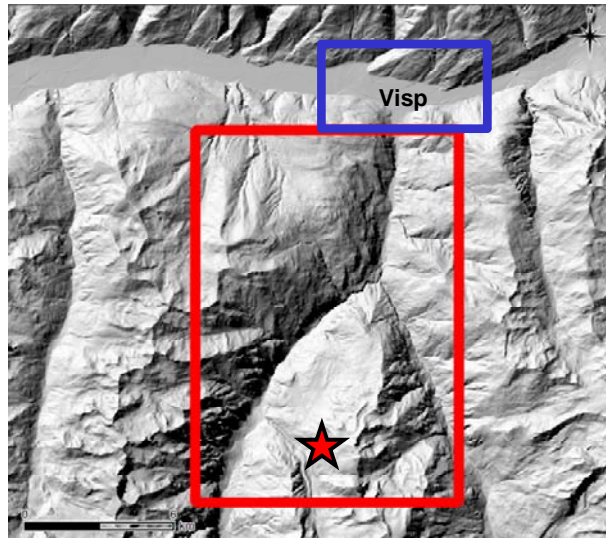
Figure 3.1: Surface projection of the proposed fault (red rectangle), study area (blue rectangle) as presented in Figures 2.1, 2.3 and 4.2. An asterisk represents the epicentre of the simulated earthquake.
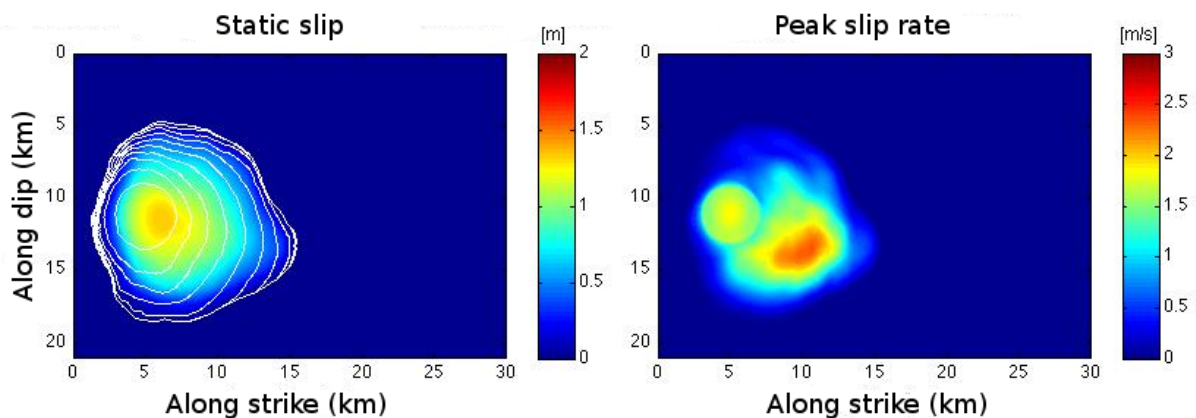

Figure 3.2: Finite source model based on the full dynamic simulation of the earthquake rupture. Static slip distribution and the contours of the rupture times (left); peak slip rate (right).

Full dynamic rupture simulations were performed using heterogeneous initial distributions, statistically compatible to the database of kinematic inversion results of past earthquakes. In particular, stress parameterization follow the methodology proposed by Dalguer and Mai (2008) to estimate the strength and initial stress on the fault prior to rupture. Their approach combines stochastic initial stress fields with a realistic fault-loading environment in which the tectonic loading regime (compressional or extensional) and the gravitational loading determine the absolute value of fault frictional resistance and initial stress. The linear slip weakening law was adopted to model the friction along the fault. Calculations were performed using the Support Operator Rupture Dynamics code (SORD). The SORD code (Ely et al., 2008, 2009) is based on a generalized Finite Difference scheme that can utilize meshes of arbitrary structure and incorporate irregular geometry. More detailed explanations of the dynamic model used here can be found in Dalguer and Mai (2011).

The dynamic simulations resulted in the finite source model, which is presented in Fig. 3.2. The model is limited up to 3 Hz. As complete slip velocity functions (SVF) were not saved during the simulation (just peak slip rates, final slip and rupture times were saved), we had to make an additional assumption on the shape of SVF. Finally, SVF was prescribed as a low-passed (2-3 Hz taper) truncated Kostrov function. The peak of such SVF was scaled to the available maximum slip rate and the duration (rise-time) was afterwards adjusted to fit the final slip.
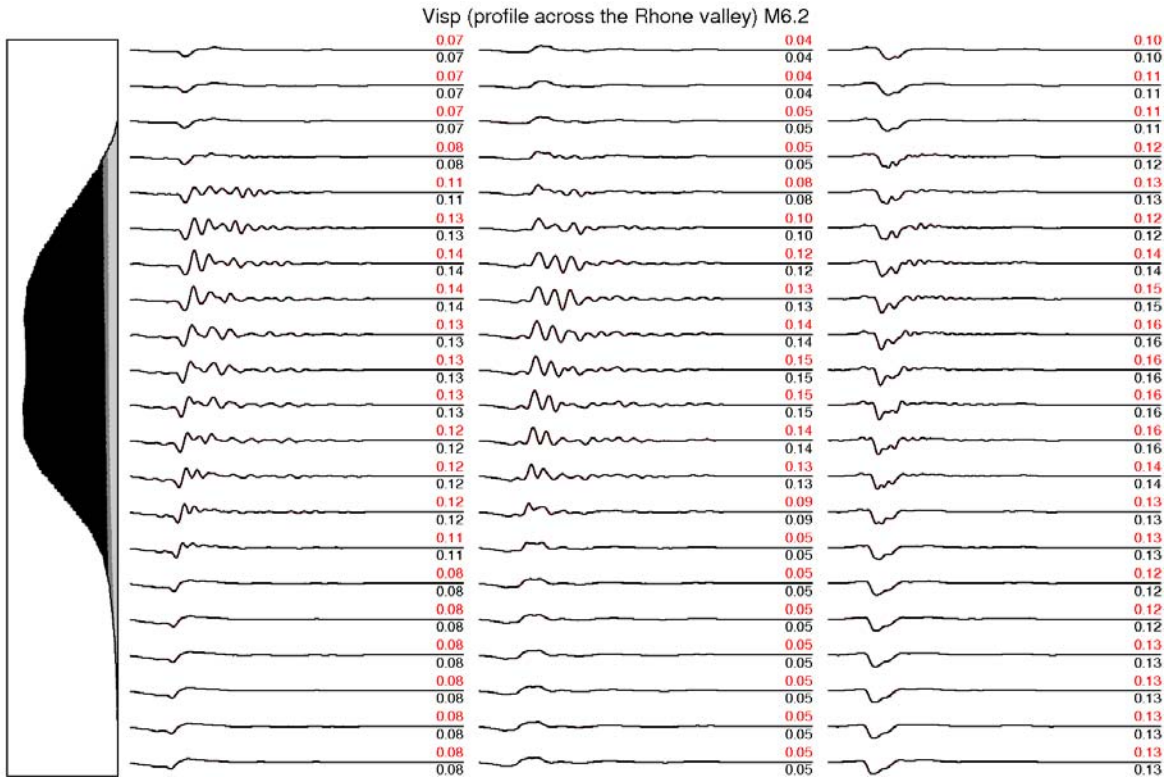
Figure 4.1: Simulated ground motion along a profile crossing Visp (see Fig. 4.2). The cross-section of the 3D model (left), velocity recordings (NS, EW, UP components respectively). The peak velocities are plotted on the right of each trace in meters per second.
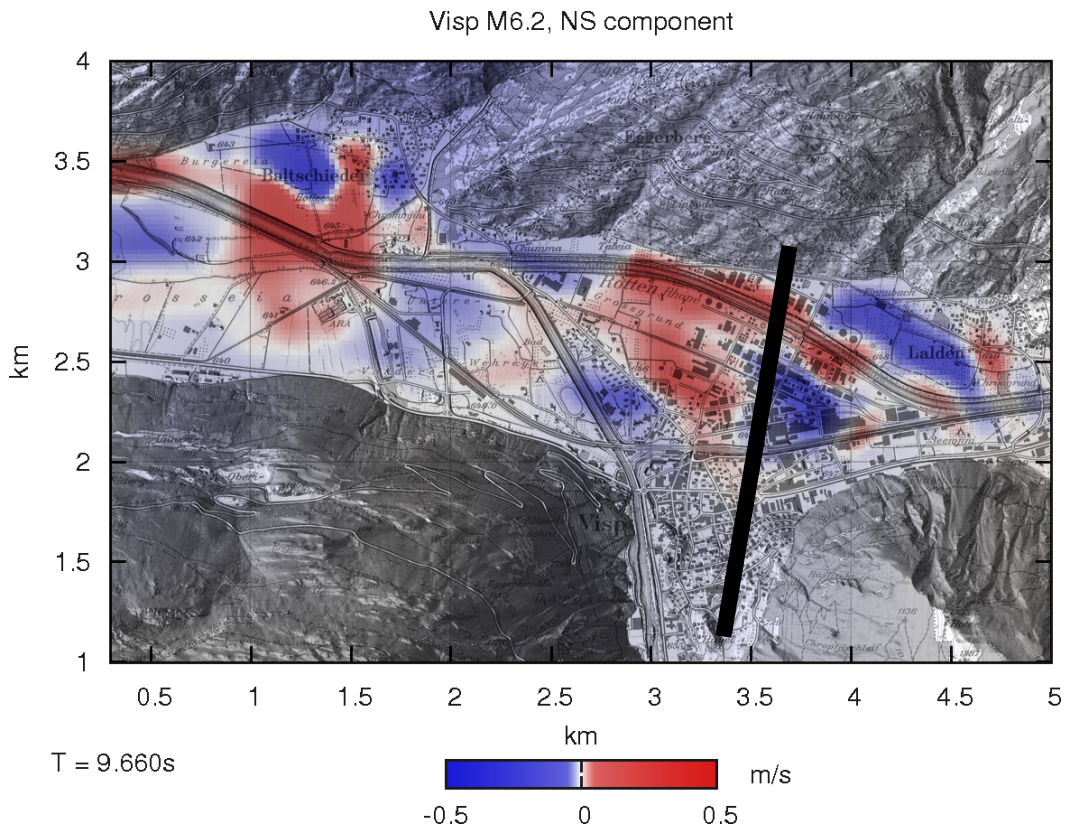

Figure 4.2: A snapshot of the ground velocity in Visp just 9.66 seconds after the earthquake origin time (approximately 3 seconds after the direct S wave arrival). The bold black line shows the location of the profile presented in Fig 4.1.

4. NUMERICAL MODELING OF GROUND MOTION

Finite difference (FD) method (Olsen, 1994; Marcinkovich and Olsen, 2003) was utilized for modelling of strong ground motion. It is a stress-velocity scheme using uniform staggered three-dimensional grid with fourth-order finite differences. Perfectly matched layers were applied on the boundary of the model, and zero-stress boundary condition on the free surface. Topography was not considered in this case. The size of the computational domain was 24x18x15 km with a spatial step of 25 m and time step of 2.5 ms. Such setup allows for modelling up to 3 Hz. A comparison with the discrete wavenumber method was performed for the reference 1D profile to test the reliability of the FD solution (not presented here). The finite source model developed in the previous section was simply incorporated into FD code as a kinematic model.

A complete presentation of the simulation results is out of the scope of this paper. We present here just synthetic seismograms for a South-North profile crossing the Visp center (Fig. 4.1) and a single snapshot of the wavefield in the basin (Fig. 4.2). Clearly, both the amplitude and duration of the simulated ground motion are higher in the center of the basin (factor of 4 in case of the peak values). Nevertheless, as the source is very close to the site, near fault effects are also very strong (e.g., vertical component in Fig. 4.1). Since the simulation does not contain frequencies above 3 Hz, no amplification is apparent in the shallow parts of the basin (fundamental frequencies > 5 Hz). The snapshot of the wavefield (Fig. 4.2) demonstrates trapping of the seismic waves in the basin. Strongest amplification was observed outside Visp in the deepest part of the basin (see Fig. 2.3).

5. DAMAGE ASSESSMENT

In a first step, in order to compute damage, the vulnerability assessment method of Lagomarsino and Giovinazzi (2006) was followed. The building stock was divided into EMS98 classes thanks to a screening survey of Visp (Michel et al., 2010).

In Lagomarsino and Giovinazzi (2006), the response of each structure is computed following a code-based approach. The period T of the structure is assessed, based on the number of stories. In case the ground motion exceeds the yield of the structure, the inelastic response is computed based on linearized value following the N2 method as implemented in EC8. The seismic behaviour of the building classes is described by bilinear capacity curves defined by a yield displacement, a yield acceleration and a ultimate displacement. They were cross-validated using empirical data (Lagomarsino and Giovinazzi, 2006). Moreover, the fragility curves for the EMS98 damage grades DG1 to DG5 are simply defined as lognormal distributions with a median for each damage grade and a lognormal standard deviation. The probability of damage grade 5 is a function of the damage distribution (Lagomarsino and Giovinazzi, 2006).

Figure 5.1: Left: Modelled expected damage (mean); Right: modelled maximum damage (80% confidence).

In a second step, fragility curves for particular building classes in Switzerland are developed (Karbassi et al., 2012), especially stone masonry structures with stiff floors and modern unreinforced masonry structures.

In practice, the elastic displacement response spectrum with 5% damping was computed from the simulated ground motion for each building location, at the building frequency. If the yield was exceeded, the inelastic displacement was computed using the N2 method. The probability of exceeding each damage grade was then computed by evaluating the lognormal cumulative density function at this displacement value. The most probable damage grade (or the median damage) and the maximum damage with 80% confidence for each building are presented in Fig. 5.1.

6. DISCUSSION AND CONCLUSIONS

A framework for the computation of earthquake scenario in Visp was established. Nevertheless further improvements are necessary. A comparison with the observed damage during the 1855 earthquake (Fritsche et al., 2006) shows obviously too low damage. This is easily explained by the fact that the modelling was performed effectively up to 2 Hz whereas most of the structures, low-rise, have a fundamental frequency greater than 3 Hz. As a conclusion, a broad-band modelling is necessary in the future to perform such scenario. Moreover, non-linear site effects has to be also incorporated in the modelling as well as fragility curves specific for Switzerland for more building classes.

REFERENCES
Baumann, C. (2012). Identification of potential faults in the Valais, COGEAR deliverable 2a.1.3, Swiss Seismological Service, Zürich, Switzerland.
Burjanek, J., G. Gassner-Stamm, and D. Fäh (2010). Array-measurements in the area of Visp and St. Niklaus, COGEAR deliverable 3.1.2, Swiss Seismological Service, Zürich, Switzerland, Report SED/COGEAR/R/003/20100226.
Burjanek, J., G. Gassner-Stamm, V. Poggi, and D. Fäh (2011). Estimation of local site effects in the Upper Valais (Switzerland). *4th IASPEI / IAEE International Symposium: Effects of Surface Geology on Seismic Motion*, In CD. University of California Santa Barbara, CA, USA.
Dalguer, L.A. and M. Mai (2008). Implications of Style-of-Faulting and Loading Characteristics on the Dynamic Rupture Process, *Eos Trans. AGU*, **89:53**, Fall Meet. Suppl., Abstract S51D-1798.
Dalguer L.A. and P. M. Mai (2011), Near- Source Ground Motion Variability from M~6.5 Dynamic Rupture Simulations. *4th IASPEI / IAEE International Symposium: Effects of Surface Geology on Seismic Motion*. In CD. University of California Santa Barbara, CA, USA.
Ely, G. P., S. M. Day, and J. B. Minster (2008). A support-operator method for viscoelastic wave modeling in 3D heterogeneous media, *Geophys. J. Int.* , **172**, 331-344.
Ely, G., S.M. Day, and J-B. Minster (2009). Dynamic rupture models for the southern San Andreas fault, *Bull. Seism. Soc. Am.*, **100:1**, 131-150.
Fäh, D., G. Stamm, and H.-B. Havenith (2008). Analysis of three-component ambient vibration array measurements, *Geophys. J. Int*, **172**, 199–213.
Fäh, D., M. Wathelet, M. Kristekova, H.-B. Havenith, B. Endrun, G. Stamm, V. Poggi, J. Burjanek, and C. Cornou (2009). Using ellipticity information for site characterization, Technical report, NERIES JRA4 Task B2.
Fritsche, S., D. Fäh, M. Gisler, and D. Giardini (2006). Reconstructing the Damage Field of the 1855 Earthquake in Switzerland: historical investigations on a well-documented event, *Geophys. J. Int.*, **166**, 719-731.
Karbassi, A., and Lestuzzi P. (2012) Seismic risk for existing buildings in Switzerland – development of fragility curves for masonry buildings, Ecole Polytechnique Fédérale de Lausanne, report prepared for the Federal Office for the Environment.
Lagomarsino, S., and Giovinazzi, S. (2006). Macroseismic and mechanical models for the vulnerability and damage assessment of current buildings. *Bulletin of Earthquake Engineering*, **4:4**, 415-443.

Marcinkovich, C. and Olsen K.B. (2003). On the implementation of perfectly matched layers in a three-dimensional fourth-order velocity-stress finite difference scheme. *Journal of Geophysical Research*, **108:B5**, 1-16.

Marschall, I., and Deichmann, N. (2012). Seismotectonics of the Valais, COGEAR deliverable 2a.1.2, Swiss Seismological Service, Zürich, Switzerland.

Maurer, H., and Kradolfer, U. (1996). Hypocentral Parameters and Velocity Estimation in the Western Swiss Alps by Simultaneous Inversion of P- and S-Wave Data, *Bull. Seism. Soc. Am.*, **86:1A**, 32-42.

Michel, C., Oropeza, M., and Lestuzzi P. (2010). Validate the building inventory and important infrastructure in the test area, COGEAR deliverable 1a.1.1, Applied Computing and Mechanics Laboratory, EPFL, Lausanne, Switzerland.

Olsen, K. B. 1994. Simulation of three-dimensional wave propagation in the Salt Lake Basin. *Ph.D. thesis*, University of Utah, Salt Lake City, Utah.

Poggi, V. and D. Fäh (2010). Estimating Rayleigh wave particle motion from three-component array analysis of ambient vibrations, *Geophys. J. Int.*, **180**, 251-267.

Poggi, V., Fäh, D., Burjánek, J., Giardini, D. (2012). The use of Rayleigh wave ellipticity for site-specific hazard assessment and microzonation. Application to the city of Lucerne, Switzerland., *Geophys. J. Int.*, **188:3**, 1154-1172.

Rosselli, A., (2001). Modelisation gravimetrique bi- et tridimensionelle du substratum rocheux des vallees alpines, *PhD thesis*, Universite de Lausanne.

Roten, D., Faeh, D., Olsen, K.B., and Giardini, D., (2008). A comparison of observed and simulated site response in the Rhone valley, *Geophys. J. Int.*, **173**, 958–978.

Roten, D., Fäh, D., Bonilla, L.F., Alvarez-Rubio, S., Weber, T.M. and Laue, I., (2009). Estimation of non-linear site response in a deep Alpine valley, *Geopys. J. Int.*, **178**, 1597-1613.

Wessel, P., and W. H. F. Smith (1998). New, improved version of the Generic Mapping Tools released, *EOS Trans. AGU*, **79**, 579.

Wathelet M. (2008). An improved neighborhood algorithm: parameter conditions and dynamic scaling, *Geophys. Res. Lett.*, **35**, L09301.

Werenfels, A. (1924). Geologische Beschreibung der Lepontinischen Alpen. Beiträge zur geologischen Karte der Schweiz, 3.Teil, Switzerland.